Journal of Photochemistry and Photobiology A: Chemistry 234 (2012) 91–99

Contents lists available at SciVerse ScienceDirect

Journal of Photochemistry and Photobiology A: Chemistry

journal homepage: www.elsevier.com/locate/jphotochem

Excitation-induced polarization decay in the plant light-harvesting complex LHCII

Alessandro Marin[a], Ivo H.M. van Stokkum[a], Vladimir I. Novoderezhkin[b], Rienk van Grondelle[a,*]

[a] Faculty of Sciences, Vrije Universiteit Amsterdam, De Boelelaan 1081, 1081 HV Amsterdam, The Netherlands
[b] A.N. Belozersky Institute of Physico-Chemical Biology, Moscow State University, Leninskie Gory, 119992 Moscow, Russia

ARTICLE INFO

Article history:
Available online 11 January 2012

Keywords:
Pump-probe
Chlorophyll
Photosynthesis
Antenna
Femtosecond
Anisotropy

ABSTRACT

The energy migration dynamics of the major light-harvesting antenna (LHCII) of plants was experimentally studied in the chlorophyll Q_y region (630–700 nm). Using polarized transient absorption (TA) spectroscopy at 77 K we obtain information unaccessible to conventional isotropic TA on the energy transfer dynamics between isoenergetic Chlorophylls (Chls). The data are simultaneously analyzed with a target analysis and interpreted in the context of the exciton model for LHCII. The transients at 652 and 662 nm excitation show that the memory of polarization is completely lost with a $(3.3–5.0\,ps)^{-1}$ rate over the whole Q_y range, which is attributed to equilibration within monomers and between the three subunits of the LHCII trimer.

1. Introduction

Photosynthesis is the complex chemical process carried out by photoautotrophic organisms that converts carbon dioxide into sugars. Light-harvesting is the initial step in photosynthesis, when solar photons are absorbed and transferred to the reaction centers running chemical reactions. In most organisms there exist protein systems dedicated to harvest light: the so-called antenna complexes. In higher plants an important role is played by the major light-harvesting complex of photosystem II (LHCII) [1–6]. This complex is the most abundant protein in the thylakoid membrane (the site of light-dependent reactions in the chloroplast) and contains about 50% of its chlorophylls (Chls). LHCII is not only an important component in light-harvesting but also plays an essential role in photoprotection [7–10]. The importance of the LHCII antenna complex requires a full knowledge of how it harvests light and transfers electronic excitations. LHCII is mainly associated with Photosystem II and consists of three similar subunits (LHCII monomers) in a trimeric structure with C_{3v} symmetry. The two Chl types it contains differ in the presence of an additional carbonyl group in Chls *b* as compared to Chls *a* and therefore in their spectral properties. The S_0–S_1 (also termed Q_y) transitions of Chls *b* and *a* absorb in the ~640–660 and 660–680 nm range, respectively. The energy transfer pathways and the corresponding excited state lifetimes are mainly determined by the mutual distance and orientation of Chls (i.e. the Chl–Chl electronic couplings) and the relative energies at which they absorb. The identification, position and orientation of all pigments were made available with the discovery of the crystal structures of LHCII at 2.72 and 2.5 Å resolution [11,12]. In each monomer six Chls *b* and eight Chls *a* are displayed in the stromal and lumenal layers, together with four Carotenoids (Cars) (cf. Fig. 1).

Since the discovery of LHCII [13,14] much effort has been devoted to resolve the energy transfer pathways in LHCII, using many experimental methods [3–5,15,16]. Early transient absorption studies revealed sub-picosecond (150–300 and 600 fs) and picosecond (4–9 ps) energy transfer components from Chls *b* to Chls *a*, and long-lived picosecond dynamics in the intermediate state region (660–670 nm) [17–20].

Palacios et al. [21] studied excitation energy transfer (EET) dynamics in LHCII with pump-probe and fluorescence experiments. Excitation was tuned to excite the Chls *b* at 650 nm and in the intermediate states a 662 nm, where both Chls *a* and red-shifted Chls *b* (at 660–665 nm) were excited. The data were characterized by both fast subpicosecond and a slower picosecond transitions for Chl *b* to *a* transfer, and by slow Chl *a* equilibration in the order of picoseconds and in 19 ps.

The correct theoretical framework able to describe transfer and spectra of strongly interacting pigments is the modified Redfield theory [22,23]. Modeling of LHCII with this approach was carried out for monomeric LHCII [24,25], and for trimeric LHCII [3,5,26–28]. The results of the calculations are described in terms of excitons (exciton representation). Excitons are a weighted superposition of Chl excited states and are calculated as the eigenstates of the

* Corresponding author. Tel.: +31 20 59 87930; fax: +31 20 444 7899.
E-mail addresses: a.marin@vu.nl (A. Marin), R.van.Grondelle@vu.nl (R. van Grondelle).

1010-6030/$ – see front matter © 2012 Elsevier B.V. All rights reserved.
doi:10.1016/j.jphotochem.2011.12.026

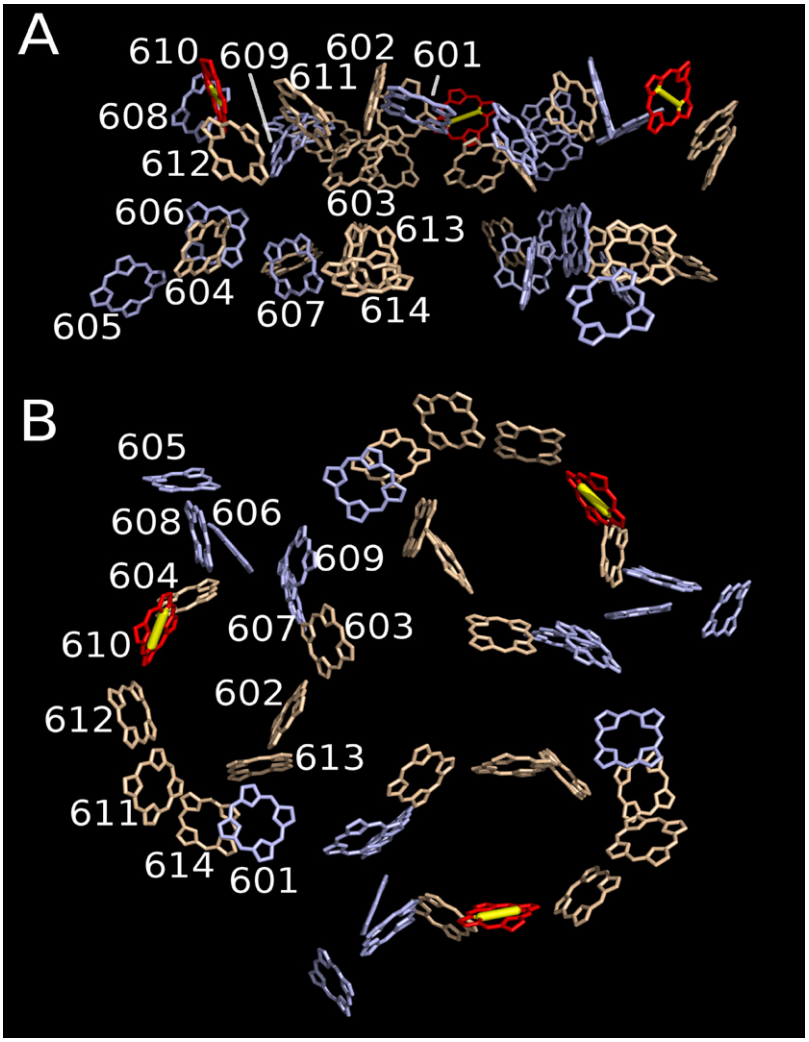

Fig. 1. Chls *a* and *b* of LHCII from the crystal structure in [11]. (A): Side view and (B) viewed from the stromal side. The final acceptors Chls *a*610 on the upper stromal layer are shown in red, and the yellow line along the NB-ND atoms depicts the orientation of the Chl Q_y dipole moment. The Chls *b* and other Chls *a* are shown in light blue and light red, respectively. Chls are labeled for one monomer. (For interpretation of references to color in this figure legend, the reader is referred to the web version of this article.)

Hamiltonian including site energies and couplings between Chls. In addition static disorder is added from which ensemble averaged spectral properties and ensemble averaged excited state dynamics can be calculated.

From the calculation of couplings between Chls, the Chls can be grouped into five strongly coupled clusters: Chl *a*604-*b*605-606-607 and *a*613-614 at the lumenal side and *b*601′-608-609, *a*602-603 and *a*610-611-612 in the stromal layer, where *b*601′ denotes Chl 601 from an adjacent LHCII monomer.

However, this theory predicts too fast transfer rates for weakly coupled and isoenergetic (clusters of) Chls. A combined Redfield–Förster approach was developed where inter-monomeric dynamics were accounted for by generalized Förster theory [5,28]. As a result, the dynamics between different dimers became slower (in the order of picoseconds or tens of picoseconds) as compared to the previous works.

In the model of Müh et al. [26,27] the Hamiltonian was calculated using quantum chemical methods, and the dynamics calculated using a combination of the Redfield and Förster approaches. Compared to [25], these works shows differences in the site energies of Chls *a*604, *b*608, *b*605 and *b*609, although the calculated dynamics in the spectral range of some of these Chls deviate from measurements. The dynamics in the Chl *a* spectral region are "slower" than in [28,29], with few subpicosecond transfers within the Chl *a*613-614 and *a*610-611-612 clusters.

Pump-probe anisotropy decays with excitation and detection in the Chl *a* Q_y as a function of temperature were measured in [30]. An anisotropy decay of 5 ± 2 ps was found at RT over the whole Chl *a* Q_y range, whereas at 13 K the decay spans from 8 to 30 ps when shifting the detection wavelength from 675 to 685 nm. Therefore, a wavelength-dependence for the anisotropy decay was found only at low temperatures. It was proposed that the slower depolarization at low temperatures was due to stronger confinement of excitations on the lowest-energy Chls *a*. The dynamics at 680 nm were consistent only with uphill transfer processes, e.g. with successive transfer between lowest energy states (at 680 nm) and mid-energy Chls *a* (at 676 nm).

Recently, in the work of Calhoun et al. [31], 2D electronic spectroscopy was applied to trimeric LHCII. The diagonal signals of nonrephasing 2D spectra were analyzed, which present quantum coherences of superpositions of excitons not disturbed by cross peaks. This led to the direct determination of the 14 exciton energies in LHCII. The results indicate that the energies are evenly distributed along the Q_y range. As compared to the energy map presented in [25], an exciton in the high-energy Chl *a* region is found at 15,130 cm^{-1}/660.9 nm, whereas an exciton

at 14,952 cm^{-1}/668.8 nm is absent. This feature was proposed to explain the fastest hundreds-of-fs EET dynamics between Chls *b* and *a* by reducing energy gaps.

Schlau-Cohen et al. [29] interpreted experimental 2D electronic spectra of LHCII in the framework of Novoderezhkin et al.'s [25] LHCII model. The data allowed the resolution of 6 cross peaks, denoting transfer between two Chl *b* and Chl *a* pools and an intermediate Chls population in the central range. Previously unobserved ultrafast dynamics (50–70 fs) from mid-energy (671–672 nm) and intermediate (662 nm) Chls *a* to the red Chls *a* (at 676 nm) were interpreted as relaxation between the two excitons with prevalent participation of the Chl *a* dimers (*a*602-603 and *a*613-614) [25]. In agreement with [28], multistep relaxation occurs from the lumenal *a*613-614 to the red states via the stromal *a*602-603 dimer. The dynamics after 300 fs can be described with a steady increase of EET to red Chls *a* and a parallel decrease of transfer to the mid-energy Chls *a*. Again, sub-100 fs dynamics were found from Chls *b*, attributed to transfer from *b*601-608-609 to the higher excitons of *a*602-603 and *a*610-611-612 trimer in the mid-energy Chl *a* range. After the depopulation of the channels to the mid-energy Chls *a* in 500 fs, a slow several-picoseconds channel from the bottleneck state Chl *a*604 to the mid-*a* Chl remains active.

The aim of this work is to further study the energy flow in LHCII and in particular among quasi iso-energetic states. To this end, we used polarized pump-probe spectroscopy at two excitation wavelenghts to excite different Chl *b*/*a* populations. For instance, excitation at 652 nm selects the Chls *b* molecules (showed in pale blue, Fig. 1), and will lead through both intra and intermonomer EET processes to a final state dominated by Chl *a*610 (Fig. 1, in red) [26,28]. Our experiments provide information on these intraband Chl *b*-Chl *b* and Chl *a*-Chl *a* dynamics, which are scarcely distinguishable in conventional isotropic pump-probe. In polarized experiments, in fact, excitation transfer among isoenergetic Chls/excitonic states of the same type generally induces a change in the orientation of the transition dipole, and therefore a change in anisotropy. We analyze the data with global and target analysis. With the latter, we describe the data with several compartments having different spectral and anisotropic properties. The aim is to capture the main features of EET, bearing in mind that EET pathways in LHCII are much more complex. We interpret the results using the model for the LHCII trimer as proposed by Novoderezhkin et al. [28].

2. Materials and methods

2.1. Sample preparation

Trimeric LHCII was prepared as described in [21]. Isolated LHCII complexes were diluted in a buffer containing 20 mM Hepes, 5 mM $MgCl_2$, 0.06% *n*-dodecyl-β-D-maltoside (pH 7.8) and 70% (v/v) glycerol for low-temperature experiments. The absorption peak in the Chl *a* Q_y was adjusted to an OD of about 0.5/mm.

2.2. Experimental setup

The pump-probe setup is described elsewhere [32]. Datasets were recorded with pump color tuned to 652 or 662 nm and excitation intensity 1.4 or 0.65 nJ/pulse, respectively. The measured spectral range was 630–695 nm with 0.83 nm resolution. At each excitation wavelength measurements were recorded with pump and probe beams oriented at parallel and perpendicular with respect to each other. In addition, with 652 nm excitation a magic angle (54.7°) dataset was recorded. All measurements were carried out at 77 K in a liquid nitrogen cryostat (Oxford DN-900, Oxford, UK). Data analysis. The relationship linking parallel and perpendicular polarized measurements to the anisotropic MA measurement reads as follows [33]:

$$\begin{aligned}\Delta A_{||}(t) &= \Delta A_{MA}(t)\cdot[1+2r(t)]\\ \Delta A_{\perp}(t) &= \Delta A_{MA}(t)\cdot[1-r(t)]\end{aligned} \quad (1)$$

where $\Delta A_{||}(t)$, $\Delta A_{\perp}(t)$ and $\Delta A_{MA}(t)$ indicate absorption difference profiles with parallel, perpendicular and magic angle polarization, respectively. Anisotropy is commonly computed from the formula:

$$r(t) = \frac{\Delta A_{||}(t) - \Delta A_{\perp}(t)}{\Delta A_{||}(t) + 2\cdot\Delta A_{\perp}(t)} \quad (2)$$

In our analysis of the 652 nm excitation data anisotropy $r(t)$ is computed from the formula:

$$r(t) = \frac{5\cdot\Delta A_{||}(t) - 4\cdot\Delta A_{\perp}(t) - \Delta A_{MA}(t)}{3\cdot\Delta A_{||}(t) + 6\cdot\Delta A_{\perp}(t) + 5\cdot\Delta A_{MA}(t)} \quad (3)$$

Eq. (3) can be verified by substituting Eq. (1) in it. It provides similar values as Eq. (2), but uses all three polarization datasets and thus is more robust for small values of $r(t)$. It is a least squares estimator for $r(t)$ which provides more precise estimates.

2.3. Global and target analysis

Global and target analysis are described in [34]. Global analysis employs a sequential scheme with increasing lifetimes to estimate Evolution Associated Difference Spectra (EADS) and associated lifetimes. For each individual excitation wavelength or polarization, four components were needed. In addition, a coherent artifact with concentration resembling the Gaussian shaped instrument response function (IRF) was used. After the global analysis of individual measurements, a simultaneous target analysis of each of the polarized TA data datasets was performed with a target kinetic model that included a description for anisotropy. The aim of target analysis is to estimate the Species Associated Difference Spectra (SADS) and concentrations of pure excited Chl states. The concentration of the *l*th species with detection at magic angle can be computed from the multiexponential decay that results from the target kinetic model convolved with the IRF and is called $c_l(t)$. Then with parallel or perpendicular detection this concentration has to be multiplied by $1+2r_l$ or $1-r_l$, respectively, where r_l is the anisotropy of the *l*th species. The contribution of the *l*th species to $\Delta A_{MA}(t)$ is the product of its concentration and its SADS: $c_l(t)\cdot SADS_l(\lambda)$. Thus the full model for the simultaneous target analysis of $\Delta A_{||}(t)$, $\Delta A_{\perp}(t)$ and $\Delta A_{MA}(t)$ reads:

$$\begin{bmatrix}\Delta A_{||}(t,\lambda)\\ \Delta A_{\perp}(t,\lambda)\\ \Delta A_{MA}(t,\lambda)\end{bmatrix} = \sum_{l=1}^{Nspecies} c_l(t)\cdot SADS_l(\lambda)\cdot\begin{bmatrix}1+2r_l\\ 1-r_l\\ 1\end{bmatrix} \quad (4)$$

Note that the anisotropy of the above mentioned coherent artifact was set to 0.4.

3. Results

3.1. Pump-probe traces

Selected pump-probe traces of the three datasets after 652 nm excitation are presented in Fig. 2. The traces at 650.3 nm show the Chl *b* dynamics after direct excitation. The Chl *b* signals decay completely in about 10 ps and display a strong subpicosecond component. The positive signal thereafter is due to the Chl *a* excited state absorption (ESA). The 669.4 nm traces were detected in the intermediate states region between the main Chl *b* and *a* bleaching. Following 652 excitation these traces show a steady increase up to 2 ps followed by de-excitation up to about 15 ps. At 677.7 nm the Chl *a*

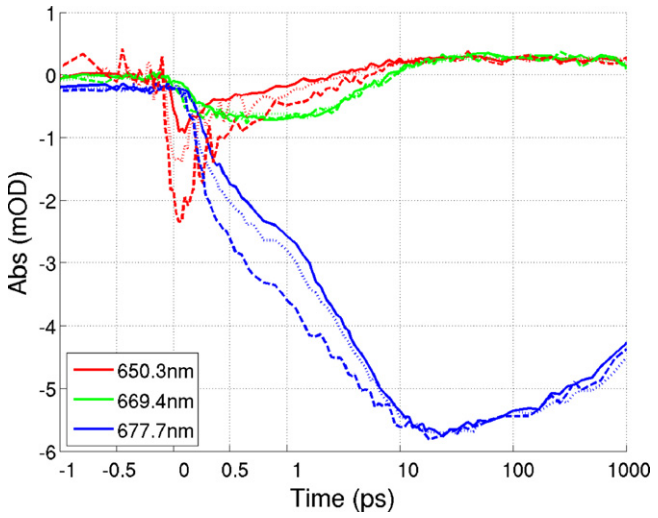

Fig. 2. Pump-probe traces at perpendicular (solid), parallel (dashed) and MA (dotted) polarizations after 652 nm excitation. The perpendicular measurement was scaled by 1.0485.

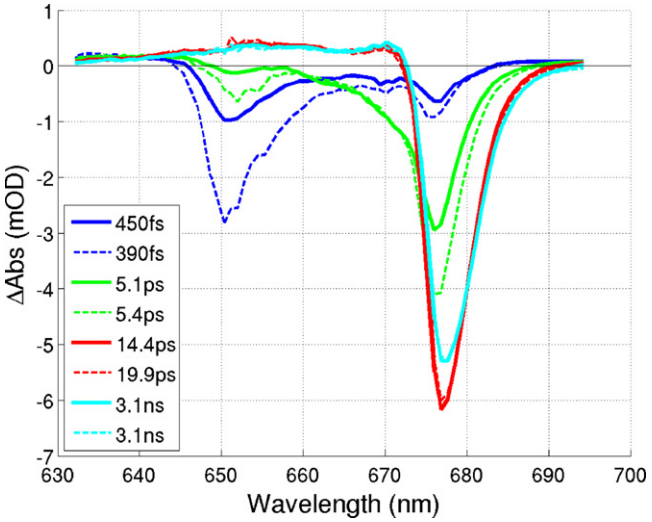

Fig. 4. EADS and lifetimes estimated from independent global analyses at perpendicular (dashed) and parallel (solid) polarizations after 652 nm excitation. The perpendicular measurement was scaled by 1.0485.

traces reach the absolute minimum ΔOD signal. These traces show a biphasic rise of the bleaching in hundreds of femtoseconds and picoseconds, and after 20 ps the Chl *a* excited states start to decay. At 3.6 ns, the longest delay time of the measurements, a fraction of Chls *a* is still excited.

The pump-probe traces after 662 nm excitation are shown in Fig. 3. The 677.2 nm traces display analogous dynamics as the 677.7 nm traces after 652 excitation (Fig. 2), except for the enhanced amplitudes immediately after excitation. In Fig. 3 the 665.5 and 668.9 nm traces in the intermediate states region, having similar shapes and amplitudes, show a bleaching at time zero followed by a decay in the picosecond time range; the redder ones have an additional small negative contribution around 1 ps denoting energy transfer.

As expected, the parallel/perpendicular polarization experiments show shortly after excitation the largest/smallest signals as compared to the other polarizations. These differences in amplitudes (and therefore anisotropy) are retained up to about 10 ps, when the signals at the different polarizations become nearly identical. In Fig. S3 more traces are shown together with the fit from the target analysis.

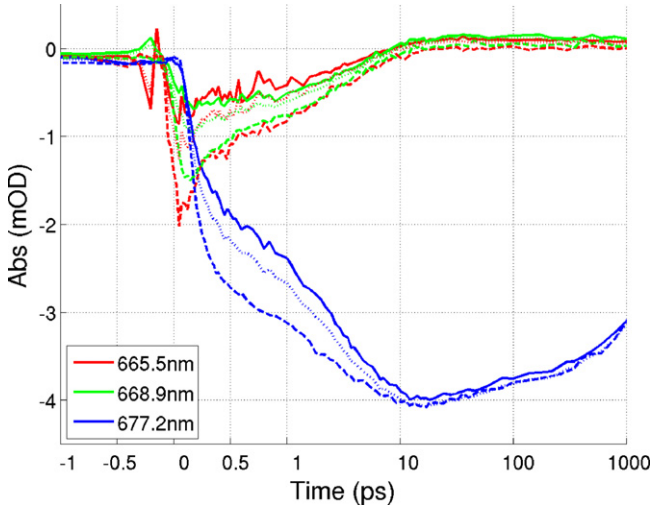

Fig. 3. Pump-probe traces at perpendicular (solid), parallel (dashed) and MA (dotted) polarizations after 662 nm excitation. The perpendicular polarization was scaled by 0.9365. The MA trace was computed for comparison with Fig. 2.

3.2. Spectral evolution after 652 nm excitation

The global analyses of the 652 nm excitation measurements are displayed in Fig. 4 (parallel and perpendicular detection) and in Fig. S2 (magic angle detection). The first spectrum shows a Chl *b* bleach at 650.3 nm and a smaller Chl *a* bleach with peaks at 670.2 and 675–676 nm. These latter Chl *a* bands are the result of some direct excitation together with some ultrafast EET. The first 390–450 fs lifetime describes the transfer of 86% Chl *b* amplitude to Chls *a*. In the second EADS a Chl *a* bleach peaks at 676–677 nm with a pronounced shoulder in the intermediate states region at 669–672 nm. The decay of the Chl *b* is completed in 5.1–5.4 ps and its center has red-shifted to 651–652 nm. In the Chl *a* region, the intermediate states at 670–672 nm decay on a similar 5 ps timescale, whereas the accepting Chls *a* peak at 676.8 nm. The 14.4–19.9 ps dynamics shows a 11–15% reduction of the Chl *a* band at low-energies possibly due to intermonomer annihilation. The long-lived excited Chls *a* peaking at 677.6 nm decay in 3.1 ns, which is the timescale of the fluorescence.

The parallel polarization measurement shows, compared to the perpendicular polarization measurement, enhanced Chl *b* and Chl *a* amplitudes in the first and second EADS. The last two EADS have similar amplitudes, meaning that depolarization is complete after the second 5.1–5.4 ps lifetime.

3.3. 662 nm excitation

The global analyses of the 662 nm excitation parallel and perpendicular measurements are shown in Fig. 5. In the first EADS a pronounced bleaching due to the excited intermediate states is present, centered at 664–667 nm. An additional small bleach can be distinguished at 657–660 nm superimposed on the Chl *a* ESA. Compared to the first spectrum of the 652 nm dataset, the same Chl *a* band at 675.5 nm is present. The first transition takes place in 250–360 fs. It shows a 75–81% reduction in the area of the intermediate states together with transfer to the species peaking at 676–677 nm. In the 3.1–3.6 ps transition a second slower phase contributes to the EET dynamics from the intermediate states to the Chls *a* at 676–677 nm. The 9.8-13.4 ps transition shows the complete decay of the intermediate states and a minor decay (6–8%)

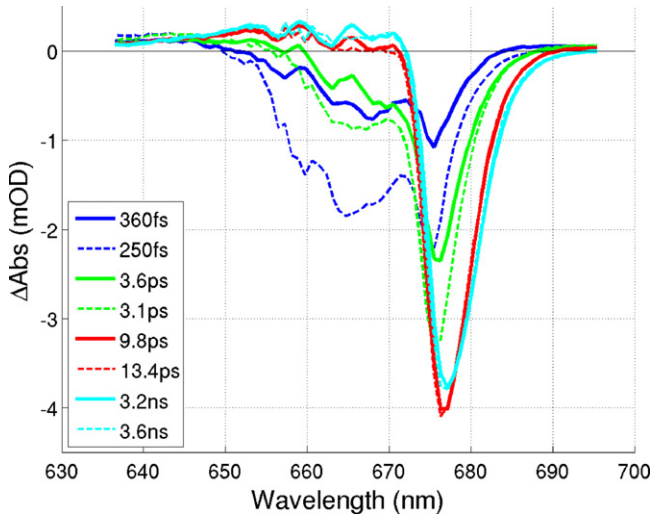

Fig. 5. EADS and lifetimes estimated from independent global analyses at perpendicular (dashed) and parallel (solid) polarizations after 662 nm excitation. The perpendicular polarization was scaled by 0.9365.

of the Chl *a* band. The long-lived Chl *a* excited states peaking at 677.6 nm decay in 3.2/3.6 ns.

Analogous to 652 excitation, the intermediate states and Chl *a* feature enhanced polarization, visible in the relative amplitudes of the first and second EADS. Also, the last two EADS have similar amplitudes, meaning that depolarization is complete after the second 3.1–3.6 ps lifetime.

3.4. Target analysis of the 652 nm dataset

Target analysis was carried out on the three 652 nm measurements with the kinetic scheme as shown in Fig. 6B. The quality of the fit of the target analysis was satisfactory, cf. Fig. S3, and increasing the complexity of the kinetic scheme did not yield to an improvement in the rms error of the fit of more than about 1%. Assumptions on spectra and parameters of the fit were needed to resolve the seven SADS (Fig. 6A). Referring to the compartmental schemes in Fig. 6B, the assumptions used are: (1) Chls b1 and b2 were zeroed above 663.0 and 661.5 nm, respectively. Chl 665 was zeroed below 662 and above 674 nm; (2) the ESA of Chl a1 and Chl a2 were equalized to the ESA of Chl a4 below 657 and 672 nm, respectively; (3) input to the kinetic scheme was given to the Chl b1 (74%) and Chl a2 (13%) compartments. These compartments had fixed 0.4 anisotropy. The remaining 13% input was given to the Chl 665 component. The Chl b2 compartment represents Chl *b* pigments with lower anisotropy, which are quickly populated from

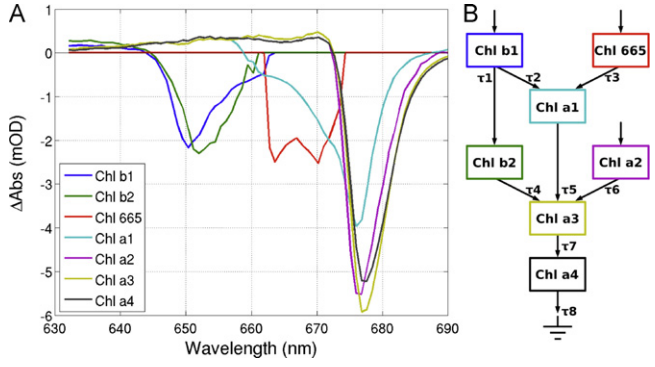

Fig. 6. (A) SADS estimated from target analysis of the 652 nm dataset. (B) Kinetic scheme.

Table 1
Reciprocal of kinetic rates.

Kinetic rate	[ps]
$\tau 1$	0.83
$\tau 2$	0.55
$\tau 3$	0.36
$\tau 4$	2.9
$\tau 5$	7.8
$\tau 6$	5.5
$\tau 7$	30.3
$\tau 8$	4490

the Chl b1 compartment. Looking at the resulting SADS, the spectral assumptions for Chl b1-b2 and Chl a1-a4 are natural, since the spectra look similar to Chl *a* or *b* bands. The SADS of Chl a1 has a long tail on the shorter wavelength side of the main Chl *a* peak. The assumptions on Chl 665 on the other hand appear rather artificial; the dynamics in the intermediate states were in fact difficult to spectrally resolve for both the 652 and 662 nm excitation datasets (vide infra).

The Chl b1 and Chl b2 compartments describe the Chl *b* dynamics with subpicosecond (Chl b1 decays in 0.36 ps) and picosecond ($\tau 4 = 2.9$ ps) phases. The slower 5.1–5.4 ps lifetime in the global analyses of Fig. 4 is probably a mixture of a 2.9 ps component and slower Chl *a* dynamics. The ≈1.3 nm red shift of the Chl *b* band in the global analysis of Fig. 4 could be reproduced in the target analysis in the SADS of the Chl b1 and b2 compartments (blue and green). The Chl 665 compartment is composed of a mixture of intermediate states and decays in $\tau 3 = 0.36$ ps to Chl a1.

Four other compartments (Chl a1, a2, a3, a4) describe the slower picosecond to nanosecond dynamics in the Chl *a* absorption region. Chl a2, receiving 13% of the total input, describes the Chl *a* species at 676–677 nm present in the spectra at time zero, in analogy to the same Chl *a* peak in the global analysis of Fig. 4. Chl a3 is populated in several picoseconds by a combination of the $\tau 4$, $\tau 5$ and $\tau 6$ channels. The effect on the SADS is analogous to the 5.1–5.4 ps transition in Fig. 4, where the intermediate states transfer to the low-energy Chls *a* at about 677 nm. Finally, two transitions showing a progressive red shift in absorption and taking place in $\tau 7 = 30.3$ ps and $\tau 8 = 4.5$ ns conclude the description of the Chl *a* decay.

The estimated anisotropy values are collated in Table 2. The anisotropies of Chl b1 and Chl a2 (both excited by the pump beam) were fixed to the maximum value of 0.4. When left free they converged to 0.44 due to experimental uncertainties or the presence of some coherences [35,36]. Chl b1 transfers to the red shifted Chl b2 and to Chl a1, concomitant with an anisotropy decrease to 0.21 and 0.04, respectively. Both Chl b2 and a1 transfer to Chl a3, which is unpolarized. The 0.31 anisotropy of the directly excited Chl 665 is close to the maximum value of 0.4.

3.5. Target analysis of the 662 nm dataset

The 662 nm excitation dataset was fitted with the six compartments depicted in the scheme of Fig. 7B. Notice that the Chl a1′-a4′ denote different species from Chl a1′-a4′ in Fig. 6. The spectral

Table 2
Anisotropy values *r* for each compartment in Fig. 6B (see Eq. (4)).

Compartment	Anisotropy
Chl b1	0.4
Chl b2	0.21
Chl 665	0.31
Chl a1	0.04
Chl a2	0.4
Chl a3	0
Chl a4	0

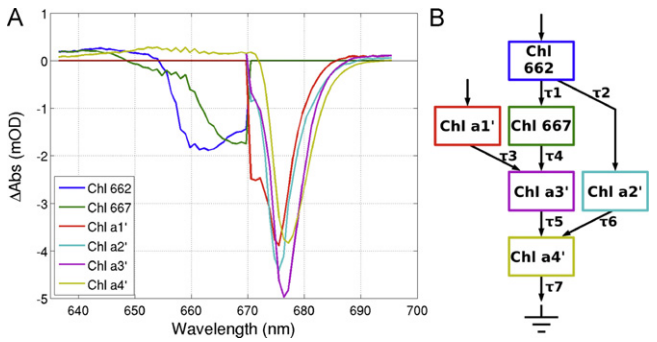

Fig. 7. (A) SADS estimated from target analysis of the 662 nm dataset. (B) Kinetic scheme.

Table 3
Reciprocal of kinetic rates.

Kinetic rate	[ps]
$\tau 1$	0.43
$\tau 2$	0.74
$\tau 3$	0.47
$\tau 4$	4.3
$\tau 5$	5.6
$\tau 6$	3.8
$\tau 7$	3570

assumptions made are: (1) The ESA of the Chl a2′-a4′ compartments were equalized below 670 nm, and Chl a1′ was zeroed in that region; (2) Chl 662 and Chl 667 were zeroed above 670 nm; (3) The Chl 662 and Chl a1′ compartments receive 65% and 35% input, respectively, whereas Chl 667 is populated by Chl 662, and contains pigments with lower anisotropy. In the 670–672 nm range the overlapping SADS could not be properly resolved.

The Chl 662 compartment contains the intermediate states (654–670 nm), it decays in 0.27 ps evolving to the Chl 667 and Chl a2′ compartments with lifetimes $\tau 1 = 0.43$ ps and $\tau 2 = 0.74$ ps (Table 3). The spectra of Chl 662 and Chl 667 mimic the decay of intermediate state species in two phases. Finally, Chl a1′-a3′ describe the dynamics of the low-energy Chls *a*, showing a progressive red shift in absorption.

The directly excited compartments Chl 662 and Chl a1′ have anisotropies smaller than 0.4, (0.33 and 0.28, respectively). This is an indication that the fastest kinetic processes are not being resolved with the time resolution of our measurements. Remarkably, Chl a2′ which receives input from Chl 662 still possesses a high anisotropy of 0.28. In contrast, Chl 667 which also receives input from Chl 662 shows an expected decay of the anisotropy to 0.13 (cf. Table 4). Finally, Chl a3′ and a4′ have zero anisotropy.

Table 4
Anisotropy values *r* for each compartment in Fig. 7B (see Eq. (4)).

Compartment	Anisotropy
Chl 662	0.33
Chl 667	0.13
Chl a1′	0.28
Chl a2′	0.28
Chl a3′	0
Chl a4′	0

3.6. Anisotropy profiles

Anisotropy profiles as a function of time probed at the maximum Chl Q_y are shown for the 652 (Fig. 8, left) and 662 nm (Fig. 8, right) excitation datasets. The profile after 652 nm excitation (Fig. 8, left) start at time zero with a value of $r = 0.38$ and decays within ≈10 ps. This anisotropy profile can be considered zero at about 25 ps, and at 10 ps the anisotropy has a value of $r = 0.05$, meaning that at this delay time anisotropy has almost completely vanished.

The profile at 677.2 nm (Fig. 8, right) has an initial anisotropy of ≈0.17 decaying at 10 ps to a value of $r = 0.04$. The small initial value can be explained by depolarization processes faster than ∼100 fs that are not being resolved or by the counteracting contributions of the coherent artifact and the Chls *a*. As after 652 nm excitation (Fig. 8, left), at about 25 ps the signal is completely unpolarized.

4. Discussion

4.1. Anisotropy vanishes at long delay times

In the anisotropy profiles of Fig. 8 anisotropy reaches at long time delays a zero value after both 652 and 662 nm excitation. This residual zero anisotropy has two origins: (1) the angle between the optical transitions at 652/662 nm and the accepting transitions at 670/680 nm and (2) intermonomer energy transfer among the lowest-energy states of the LHCII trimer (see Fig. 1). The tilt of the lowest-energy states (mainly Chls *a*610, cf. Fig. 1) is such that equilibration from the excited Chls (e.g. the Chls *b* after 652 nm excitation, cf. Fig. 1) results in practically zero final anisotropy.

The fact that the residual anisotropy is zero is also confirmed by the LD spectrum, which depends on the angle θ between the transition dipoles and the axis perpendicular to the membrane plane by $LD \propto [3\cos^2(\theta) - 1]$. The 670–680 nm band in fact shows a positive contribution to the LD spectrum and is therefore polarized more or

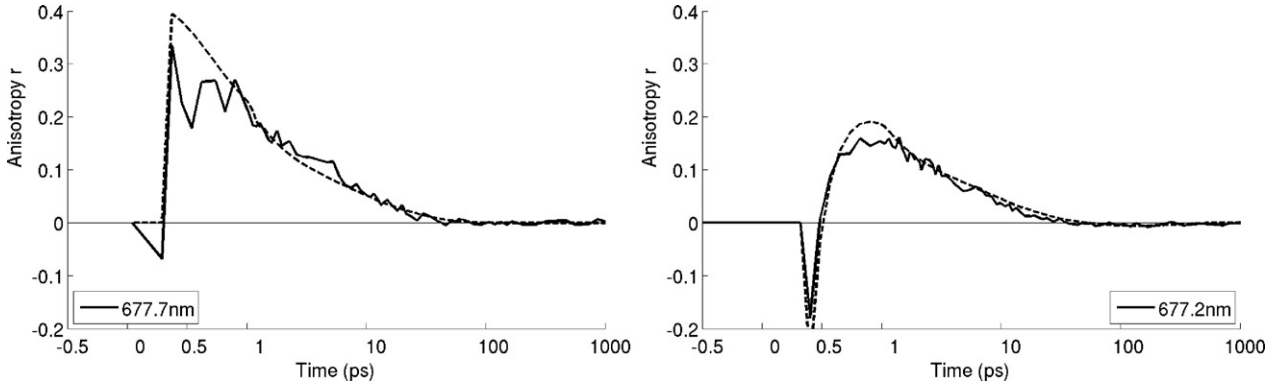

Fig. 8. 77 K anisotropy profiles $r(t)$ after 652 nm excitation at 677.7 nm (left) and after 662 nm excitation at 677.2 nm (right). Dashed lines indicate the target analysis fits. The profiles are shown after time zero and up to 1 ns.

less in the membrane plane. On the other hand, the contributions from the 650 to 660 nm region cancel out to nearly zero, thus the corresponding transitions are on average oriented neither in the membrane plane, nor oriented normal to the plane where the LD is negative. [37,38] Therefore, selective excitation of the 650–660 nm region should give near to zero anisotropy in the 670–680 nm region after equilibration among the three final acceptors.

Direct excitation of the 675–685 nm band yielded in Savikhin et al. 0.1 or higher residual anisotropy [30]. As expected, increasing the excitation wavelength, the more red absorbing final Chl *a* acceptors are preferentially excited and excitations maintain a certain degree of orientation which is reflected in non-zero anisotropy. In the extreme case of 685 nm excitation (and at low temperatures) only the most red absorbing final acceptors are photoselected, and a very high final anisotropy of 0.4 is obtained [30]. In that case hardly any depolarization takes place, because there is little to no energy transfer among the three final acceptors.

4.2. Anisotropy decays with a 3.3–5.0 ps lifetime

We estimate the anisotropy decay lifetime by approximating the anisotropy decays with a single exponential. We find that the profiles at 677.7 and 677.2 nm after 652 and 662 nm excitation (Fig. 8) reach $1/e$ of the initial signal at 3.3 and 5.0 ps, respectively.

The anisotropy measurements on LHCII of Savikhin et al. [30] employing single excitation and detection wavelengths yielded an anisotropy decay rate at 680 nm of $(11–17\ \text{ps})^{-1}$ between 50 and 100 K. These smaller decay rates can be explained by the different excitation wavelengths in [30] where the Chl *a* Q_y wavelength range from 675 to 685 nm was scanned, implying excitation of only the lowest energetic states. In turn, our faster anisotropy decay rates at 652 and 662 nm excitation are determined by the transitions from Chls *b* and Chls *b*/*a* in the intermediate states, whereas in [30] these states were not photoselected. We imply that the dominant depolarization processes from these Chl states occur mainly within an LHCII monomer (intramonomeric EET), corresponding to the sub-picosecond τ1–τ2–τ3 transitions in the target analyses (Figs. 6 and 7). This interpretation is also in agreement with the higher residual anisotropy found by the same authors after excitation in the Chl *a* Q_y band.

Consistent with [30], also in our anisotropy profiles the redder excitation yields a longer anisotropy decay time (3.3 and 5.0 ps after 652 and 662 nm excitation, respectively). This suggests that the tail of the anisotropy decay contains a relatively slow (picoseconds) contribution. In the target analysis these transitions are possibly described by the 5.5–7.8 ps ($\tau5$–$\tau6$ in Fig. 6) and 3.8–4.3 ps ($\tau4$–$\tau6$ in Fig. 7) transitions at 652 and 662 nm excitation, respectively. Fitting the tail of the 677.7 and 677.2 nm anisotropy profiles yields a similar lifetime (8.7 ± 0.2 and 7.3 ± 0.4 ps, not shown). These lifetimes, considering the work of Lyle and Struve [39] (see below in this paragraph), agree with the estimated intermonomeric hopping time of about 20 ps [28]. Therefore, the slow (picosecond) decay in the anisotropy profiles are mainly due to EET between Chls *a* of different monomeric subunits (intermonomeric EET).

Lyle and Struve showed that in a trimeric complex of identical chromophores with C_{3v} symmetry anisotropy decays with a rate three times larger that the one describing EET [39]. Therefore, the overall inverse rate constant for EET in a LHCII trimer would be between 10 and 15.0 ps at 652 and 662 nm excitation, respectively. Note that these rates correspond to the slowest picosecond Chl *a* equilibrations found for trimeric LHCII [18,20]. However, also in monomeric LHCII and the minor complexes slow picosecond phases [40,41], when excitations equilibrate on the lowest energy Chls *a*. Consequently, to truly assign the depolarization dynamics in LHCII in terms of intra-monomer and inter-monomer EET the full Redfield model must be solved (see [5,28]).

4.3. Chl b dynamics

The Chl *b* bleaching decays in two phases (cf Fig. 4): the major one in the subpicosecond time scale (390–450 fs) accounts for the 86% of the bleaching. In [21] however, two subpicosecond components of ≈130 and 600 fs were present. We could not find evidence for this by fitting the 620–660 nm region (not shown), but the 0.38–0.45 ps lifetimes found in Fig. 4 seem to be an 'average' of the ones found in [21]. This behavior is very similar to what was found in reconstituted minor complexes, where lifetimes of 0.21/0.61 and 1.5/3.6 ps were extracted for CP26/CP24 [41]. In the target analysis of Fig. 5 the Chl *b* dynamics were modeled with two compartments. The fast phase is accounted for by Chl b1 decaying in 0.33 ps (the sum of the $\tau1$ and $\tau2$ rates in Table 1), whereas the slow decay is modeled by the slow $\tau4 = 2.9$ ps decay from Chl b2 to Chl a3.

In the excitonic model of Novoderezhkin et al. [28] EET from Chls *b* consists in a subpicosecond (300–800 fs) transfer between the Chl *b*601′-608-609 cluster and the stromal Chls *a* clusters (i.e. *a*602-603 and *a*610-611-612), and a fast (100–200 fs) equilibration within the lumenal *a*604-*b*605-*606*-607 cluster resulting in the population of the bottleneck *a*604 state. These fast dynamics are caught by the target analysis of Fig. 6A and describe the decay of Chl b1, although in the exciton model two Chl *b* clusters are decaying in parallel.

The lifetime between the two Chl b1 and b2 compartments in the target analysis of Fig. 5 is $\tau1 = 0.83$ ps, in agreement with [29], where the cross peak (649.3 nm, 649.3 nm) corresponding to Chl *b* to Chl *b* transfer almost completely disappears in 1 ps. In the transition from Chl b1 to Chl b2 a red shift of the Chl *b* absorption bands takes place, which is also visible in the first phase in the global analysis of Fig. 4. This equilibration within Chl *b* pools might correspond to relaxation within the lumenal and stromal Chl *b* pools (corresponding to the k14-k10/k14-k9 and k13-k12/k13-k11, although they were given faster (50–800 fs) kinetics).

In [29] evidence was found for ultrafast EET from Chl *b* to mid-Chl *a* at 671.1 nm and to Chl *a* at 678.2 nm. Energy transfer to these species is modeled with a sub-picosecond time scale by the Chl b1 to a1 transition ($\tau2 = 0.55$ ps). The ultrafast dynamics in [29] might be reflected in our data by the presence of two bands at 670 and 675–676 nm in the first EADS of Fig. 4, and would be modeled in the target analysis by giving input to the Chl 665 and Chl a2 compartments, respectively. These dynamics can be attributed to sub-picosecond relaxation between the stromal *b*601′-608-609 cluster (excitons k13, k12) and the excitons highest in energy with predominant participation of *a*610-611-612 and *a*602-603 (excitons k8 and k6, respectively).

The slow Chl *b* decay is described by the $\tau4 = 2.9$ ps decay of the Chl b2, and can be assigned to the slow EET dynamics in the lumenal side from Chl *b*605 to Chl *a*604. This transition from Chl 605 to Chl 604 would yield a 111° change in the orientation of the dipole moment with a shift to negative anisotropy.

4.4. Dynamics in the intermediate state region

The fastest dynamics in the 660–672 nm region after 652 nm excitation is accounted for by the $\tau3 = 0.36$ ps lifetime of Chl 665 (Fig. 6, Table 2). The SADS of Chl 665 hosts the absorption of excitons k8 (Chls *a*611-612) at 666.3 nm, k6 (Chls *a*602-603) and k5 (Chl *a*613-614) around 670 nm (cf Fig. S1). In [29] this region showed pronounced sub-100 fs EET dynamics of the the mid-*a* Chls (671.1 nm), and in the exciton model these excitons decay with dynamics ranging from ultrafast (e.g. k8–k2 and k1 in 50–80 fs) to hundreds of femtoseconds (k8–k6 in 325 fs, k6–k4 or k2 in 400 fs, k5–k3 in 155 fs) [28]. Therefore, it is probable that the experiments of [29] detect the fast sub-100 fs transition (e.g. the ones within the stromal Chl *a*610-611-612 trimer, k8 to k2 and k1),

whereas in our data we mimic these transitions by giving input to Chl a2 in Fig. 6B.

In the target analysis for the 662 nm dataset (Fig. 7) the fastest dynamics in the intermediate states are described by the 0.27 ps decay (the sum of $\tau 1$ and $\tau 2$) of Chl 662 (Fig. 7B, Table 3). These transitions include relaxation between the k6–k4 and k5–k3 excitons, i.e. excitons with high spatial overlap on the *a*602-603 and *a*613-614 dimers, respectively.

In addition, the Chl 662 nm experiment very likely contains excited Chls *b*, as it was found for reconstituted CP26 and CP24 at the same excitation wavelength [41]. The Chl *b* part of the bleaching, which is most visible in the blue part of the bleaching in the first EADS of Fig. 5, is likely the effect of Chl *b*605 to *a*604 relaxation (exciton k9 to k7). On the other hand, the lifetime that was calculated for this process is one order of magnitude larger than $\tau 1 = 0.43$ ps [28]. Another candidate could be Chl *b*607 (exciton k10), which is also populated around 660 nm, though in smaller amount than Chl *b*605 (exctiton k9) [28].

The slower dynamics in the intermediate states are present in the $\tau 5 = 7.8$ ps decay of Chl a1 (Fig. 6) and in the $\tau 4 = 4.3$ ps decay of Chl 667 (Fig. 7). The transition Chl a1 to a3 reflects a combination of several processes: transfer from the bottleneck state Chl *a*604 (exciton k7) to the lumenal dimer (excitons k5/k3); transfer between the luminal dimer *a*613-614 and the stromal *a*602-603 and *a*610-611-612 clusters.

4.5. Dynamics in the Chl a range

In the 652 nm dataset (Fig. 6) the Chl *a* region is described by slow picosecond ($\tau 5 = 7.8$ ps, $\tau 6 = 5.5$ ps), tens of picoseconds ($\tau 7 = 30.3$ ps) and nanosecond lifetimes (reflecting the Chl fluorescence decay $\tau 8 = 4.5$ ns).

Chl a2 in the 652 nm dataset (Fig. 6) and Chl a1′-a2′ in the 662 nm dataset (Fig. 7) decay with a small red-shift from 675.5 to 676–677 nm. The peak at 675.5 nm, also present in the 652 nm data (Fig. 4), corresponds to exciton k4 and k3, i.e. the lowest excitons of the 602/603 and 613/614 dimers mostly localized on Chl *a*602 and *a*613, respectively. The k3 exciton was shown to relax very slowly (in about 15–20 ps, [28]) to the stromal *a*602″-603″ dimer of an adjacent monomer. This slow intra-monomeric transfer is similar to the third 14.4–19.9 and 9.8–13.4 ps transition in the global analysis (Figs. 4 and 5).

Complete equilibration of the reddest Chl *a* states is reached with the transitions to the Chl a4 and a4′ compartments. In particular, the last $\tau 7 = 30.3$ ps transition from Chl a3 to Chl a4 in Fig. 6 reflects the very slow excitation flow between Chl *a* clusters following relaxation of the lumenal Chl *a*604 bottleneck state.

Acknowledgments

We thank H. van Roon for sample preparation and Jos Thieme for technical support. This work was supported by the Netherlands Organisation for Scientific Research (NWO)–Chemical Sciences (CW) through a TOP grant 700.58.305 to RvG and by the European Research Council (ERC) through Advanced grant proposal no 267333 (PHOTPROT) to RvG. VN was supported by a visitor's grant from the Netherlands Organisation for Scientific Research (NWO), Grant No. 040.11.207 and by the Russian Foundation for Basic Research, Grant No. 09-04-00605.

Appendix A. Supplementary data

Supplementary data associated with this article can be found, in the online version, at doi:10.1016/j.jphotochem.2011.12.026.

References

[1] R.E. Blankenship, Molecular Mechanisms of Photosynthesis, Blackwell Science, Oxford malden, MA, 2002.
[2] J. Nield, J. Barber, Refinement of the structural model for the Photosystem II supercomplex of higher plants, Biochim. Biophys. Acta 1757 (2006) 353–361.
[3] R. van Grondelle, V.I. Novoderezhkin, Energy transfer in photosynthesis: experimental insights and quantitative models, Phys. Chem. Chem. Phys. 8 (2006) 793–807.
[4] H. van Amerongen, R. van Grondelle, Understanding the energy transfer function of LHCII, the major light-harvesting complex of green plants, J. Phys. Chem. B 105 (2001) 604–617.
[5] V.I. Novoderezhkin, R. van Grondelle, Physical origins and models of energy transfer in photosynthetic light-harvesting, Phys. Chem. Chem. Phys. 12 (2010) 7352–7365.
[6] G.D. Scholes, G.R. Fleming, A. Olaya-Castro, R. van Grondelle, Lessons from nature about solar light harvesting, Nat. Chem. 3 (2011) 763–774.
[7] A.V. Ruban, A.J. Young, P. Horton, Modulation of chlorophyll fluorescence quenching in isolated light harvesting complex of Photosystem II, Biochim. Biophys. Acta 1186 (1994) 123–127.
[8] N.E. Holt, D. Zigmantas, L. Valkunas, X.-P. Li, K.K. Niyogi, G.R. Fleming, Carotenoid cation formation and the regulation of photosynthetic light harvesting, Science 307 (2005) 433–436.
[9] A.V. Ruban, R. Berera, C. Ilioaia, I.H.M. van Stokkum, J.T. Kennis, A.A. Pascal, H. van Amerongen, B. Robert, P. Horton, R. van Grondelle, Identification of a mechanism of photoprotective energy dissipation in higher plants, Nature 450 (2007) 575–578.
[10] S. Bode, C.C. Quentmeier, P.-N Liao, N. Hafi, T. Barros, L. Wilk, F. Bittner, P.J. Walla, On the regulation of photosynthesis by excitonic interactions between carotenoids and chlorophylls, Proc. Natl. Acad. Sci. U.S.A. 106 (2009) 12311–12316.
[11] Z.F. Liu, H.C. Yan, K.B. Wang, T.Y. Kuang, J.P. Zhang, L.L. Gui, X.M. An, W.R. Chang, Crystal structure of spinach major light-harvesting complex at 2.72 Å resolution, Nature 428 (2004) 287–292.
[12] R. Standfuss, A.C.T. van Scheltinga, M. Lamborghini, W. Kühlbrandt, Mechanisms of photoprotection and nonphotochemical quenching in pea light-harvesting complex at 2.5 Å resolution, EMBO J. 24 (2005) 919–928.
[13] T. Ogawa, F. Obata, K. Shibata, Two pigment proteins in spinach chloroplasts, Biochim. Biophys. Acta 112 (1966) 223–234.
[14] J.P. Thornber, C.A. Smith, J.L. Bailey, Partial characterization of two chlorophyll–protein complexes isolated from spinach–beet chloroplasts, Biochem. J. 100 (1966) 14–15.
[15] R. van Grondelle, Excitation energy transfer, trapping and annihilation in photosynthetic systems, Biochim. Biophys. Acta 811 (1985) 147–195.
[16] R. van Grondelle, J.P. Dekker, T. Gillbro, V. Sundström, Energy-transfer and trapping in photosynthesis, Biochim. Biophys. Acta 1187 (1994) 1–65.
[17] S.L.S. Kwa, H. van Amerongen, S. Lin, J.P. Dekker, R. van Grondelle, W.S. Struve, Ultrafast energy transfer in LHC-II trimers from the Chl a/b light-harvesting antenna of Photosystem II, Biochim. Biophys. Acta 1102 (1992) 202–212.
[18] H.M. Visser, F.J. Kleima, I.H.M. van Stokkum, R. van Grondelle, H. van Amerongen, Probing the many energy-transfer processes in the photosynthetic light-harvesting complex II at 77 K using energy-selective sub-picosecond transient absorption spectroscopy, Chem. Phys. 210 (1996) 297.
[19] J.P. Connelly, M.G. Müller, M. Hucke, G. Gatzen, C.W. Mullineaux, A.V. Ruban, P. Horton, A.R. Holzwarth, Ultrafast spectroscopy of trimeric light-harvesting complex II from higher plants, J. Phys. Chem. B 101 (1997) 1902.
[20] F.J. Kleima, C.C. Gradinaru, F. Calkoen, I.H.M. van Stokkum, R. van Grondelle, H. van Amerongen, Energy transfer in LHCII monomers at 77 K studied by sub-picosecond transient absorption spectroscopy, Biochemistry 36 (1997) 15262.
[21] M.A. Palacios, J. Standfuss, M. Vengris, B.F. van Oort, I.H.M. van Stokkum, W. Kühlbrandt, H. van Amerongen, R. van Grondelle, A comparison of the three isoforms of the light-harvesting complex II using transient absorption and time-resolved fluorescence measurements, Photosynth. Res. 88 (2006) 269–285.
[22] A.G. Redfield, On the theory of relaxation processes, IBM J. Res. Develop. 1 (1957) 19–31.
[23] A.G. Redfield, The theory of relaxation processes, Adv. Magn. Res. 1 (1965) 1–32.
[24] V.I. Novoderezhkin, M.A. Palacios, H. van Amerongen, R. van Grondelle, Energy-transfer dynamics in the LHCII complex of higher plants: modified Redfield approach, J. Phys. Chem. B 108 (2004) 10363–10375.
[25] V.I. Novoderezhkin, M.A. Palacios, H. van Amerongen, R. van Grondelle, Excitation dynamics in the LHCII complex of higher plants: modeling based on the 2.72 Ångstrom crystal structure, J. Phys. Chem. B 109 (2005) 10493–10504.
[26] F. Müh, M.E.A. Madjet, T. Renger, Structure-based identification of energy sinks in plant light-harvesting complex II, J. Phys. Chem. B 114 (2010) 13517–13535.
[27] T. Renger, M.E. Madjet, A. Knorr, F. Müh, How the molecular structure determines the flow of excitation energy in plant light-harvesting complex II, J. Plant Physiol. 168 (2011) 1497–1509.
[28] V.I. Novoderezhkin, A. Marin, R. van Grondelle, Intra- and inter-monomeric transfers in the light harvesting LHCII complex: the Redfield–Förster picture, Phys. Chem. Chem. Phys. 13 (2011) 17093–17103.
[29] G.S. Schlau-Cohen, T.R. Calhoun, N.S. Ginsberg, E.L. Read, M. Ballottari, R. Bassi, R. van Grondelle, G.R. Fleming, Pathways of energy flow in LHCII from two-dimensional electronic spectroscopy, J. Phys. Chem. B 113 (2009) 15352–15363.

[30] S. Savikhin, H. van Amerongen, S.L.S. Kwa, R. van Grondelle, W.R. Struve, Low-temperature energy-transfer in LHC-II trimers from the Chl-a/b light-harvesting antenna of photosystem-II, Biophys. J. 66 (1994) 1597–1603.
[31] T.R. Calhoun, N.S. Ginsberg, G.S. Schlau-Cohen, Y.C. Cheng, M. Ballottari, R. Bassi, G.R. Fleming, Quantum coherence enabled determination of the energy landscape in light-harvesting complex II, J. Phys. Chem. B 113 (2009) 16291–16295.
[32] A. Marin, A.B. Doust, G.D. Scholes, K.E. Wilk, P.M.G. Curmi, I.H.M. van Stokkum, R. van Grondelle, Flow of excitation energy in the cryptophyte light-harvesting antenna phycocyanin 645, Biophys. J. 101 (2011) 1004–1013.
[33] J.R. Lakowicz, Principles of Fluorescence Spectroscopy, 3rd ed., Springer, 2006.
[34] I.H.M. van Stokkum, D.S. Larsen, R. van Grondelle, Global target analysis of time-resolved spectra, Biochim. Biophys. Acta 1657 (2004) 82–104.
[35] M. Wendling, F. van Mourik, I.H.M. van Stokkum, J.M. Salverda, H. Michel, R. van Grondelle, Low-intensity pump-probe measurements on the B800 band of *Rhodospirillum molischianum*, Biophys. J. 84 (2003) 440–449.
[36] V. Novoderezhkin, M. Wendling, R. van Grondelle, Intra- and interband transfers in the B800-B850 antenna of *Rhodospirillum molischianum*: Redfield theory modeling of polarized pump-probe kinetics, J. Phys. Chem. B 107 (2003) 11534–11548.
[37] R. Croce, R. Remelli, C. Varotto, J. Breton, R. Bassi, The neoxanthin binding site of the major light harvesting complex (LHCII) from higher plants, FEBS Lett. 456 (1999) 1–6.
[38] H. Van Amerongen, S.L.S. Kwa, B.M. van Bolhuis, R. van Grondelle, Polarized fluorescence and absorption of macroscopically aligned light-harvesting complex-II, Biophys. J. 67 (1994) 837–847.
[39] P.A. Lyle, W.S. Struve, Dynamic linear dichroism in chromoprotein, Photochem. Photobiol. 53 (1991) 359–365.
[40] A. Marin, F. Passarini, R. Croce, R. van Grondelle, Energy transfer pathways in the CP24 and CP26 antenna complexes of higher plant photosystem II: a comparative study, Biophys. J. 99 (2010) 4056–4065.
[41] C.C. Gradinaru, A.A. Pascal, F. van Mourik, B. Robert, P. Horton, R. van Grondelle, H. van Amerongen, Ultrafast evolution of the excited states in the Chlorophyll a/b complex CP29 from green plants studied by energy-selective pump-probe spectroscopy, Biochemistry 37 (1998) 1143–1149.